Complementing CGM with Sentinel-1 InSAR data

Report for SCEC Award # 17046
Submitted Aug, 2018

Investigator: Yuri Fialko (SIO/UCSD)

I. Project Overview

Abstract

The SCEC Community Geodetic Model (CGM) aims to describe surface deformation in Southern California at highest possible spatio-temporal resolution and accuracy. This requires an optimal integration of GPS and InSAR data. Over the time span of SCEC5, there will be a dramatic increase in the amount of InSAR data thanks to the European Space Agency (ESA) mission Sentinel-1. Sentinel-1 mission will provide several key improvements over the existing InSAR data sets, including:

i) frequent and regular acquisitions. The nominal revisit time for the currently operational Sentinel-1A and 1B satellites is 6 days. This can be compared to the minimum revisit time of 35 days for the previous ESA missions such as ERS-1/2 and ENVISAT.

ii) A smaller revisit time not only improves temporal resolution, but also significantly reduces problems with decorrelation of the radar phase, and helps mitigate atmospheric artifacts by virtue of averaging.

iii) Wide-swath capability. 300-km-wide swathes of Sentinel-1 ensure a complete coverage of Southern California with just a few tracks.

iv) Uniform coverage from both ascending and descending satellite orbits. Data from two different look directions allow us to separate horizontal and vertical components of surface displacements.

Incorporation of Sentinel-1 data is therefore expected to result in a significant improvement of CGM. Over the last year we have set up a system for routine systematic processing of all Sentinel-1 data from Southern California. We also started generating higher-level products for integration into CGM.

SCEC Annual Science Highlights

Tectonic Geodesy

Exemplary Figure

Figure 2.

SCEC Science Priorities

1a, 1e, 2a

Intellectual Merits

Interferometric Synthetic Aperture Radar (InSAR) data are increasingly used to image deformation due to active faults. Frequent InSAR acquisitions are expected to provide an improved signal to noise ratio for low-amplitude deformation signals. However, we find that increasing number of radar interferograms used in the analysis of surface deformation results in the accumulation of high-frequency spatial noise, which is introduced in the time series analysis due to filtering of the radar phase prior to unwrapping. We propose a new method for "unfiltering" the filtered unwrapped radar phase. We demonstrate the feasibility of the proposed method using Sentinel-1 InSAR and Global Positioning System (GPS) data. We combine data collected by Sentinel-1 between 2014-2018 with continuous GPS measurements to calculate the three components of the surface velocity field over the southern San Andreas and San Jacinto fault zones at the resolution of InSAR data (100 m). We obtain the 3 orthogonal components of surface motion using overlapping InSAR tracks with different look geometries, together with an additional constraint provided by GPS measurements of the local azimuth of the horizontal velocity vector. We estimate both secular velocities and displacement time series. The latter are calculated by combining InSAR time series from different lines of sight with time-dependent azimuths computed using continuous GPS time series at every InSAR epoch. We use CANDIS method, a technique based on iterative common point stacking, to correct the InSAR data for tropospheric and ionospheric artifacts when calculating secular velocities and time series, and to isolate low-amplitude deformation signals in our study region. This three-component, time-dependent description of surface deformation from a combination of geodetic data sets can be used as part of the SCEC Community Geodetic Model.

Broader Impacts

Evaluation of seismic hazard is based primarily on historic seismicity and long-term fault slip rates inferred from paleoseismic data. Geodetic observations provide an important additional source of information about contemporaneous accumulation of strain in the seismogenic layer. UCERF3 model now incorporates estimates of fault slip rates based on geodetic data. A major outstanding question is whether geodetic observations can help identify areas of seismic hazard that haven't been recognized based on available seismic and geologic data. While mature faults such as the San Andreas fault by and large have clear expression in geomorphology, young developing faults and fault zones may be more difficult to recognize. Sentinel-1 InSAR data will help us better understand a potential contribution of geodetic observations to estimates of seismic hazard such as UCERF. The proposed collection and analysis of space geodetic data will improve our understanding of the associated seismic hazard to populated areas in Southern California. This project has provided training and support for one graduate student.

Project Publications

Tymofyeyeva, K. and Y. Fialko, Geodetic evidence for a blind fault segment at the Southern end of the San Jacinto Fault Zone, J. Geophys. Res., 123, 878-891, 2018.

II. Technical Report

InSAR measurements of low-amplitude (sub-centimeter) deformation are chiefly limited by contributions to the radar phase due to ionosphere, troposphere, and imprecise knowledge of satellite orbits (*Goldstein* 1995; *Jehle et al.* 2010; *Meyer* 2011; *Tarayre and Massonnet* 1996; *Zebker et al.* 1997). The ionospheric phase delays are caused by the varying density of charged particles at
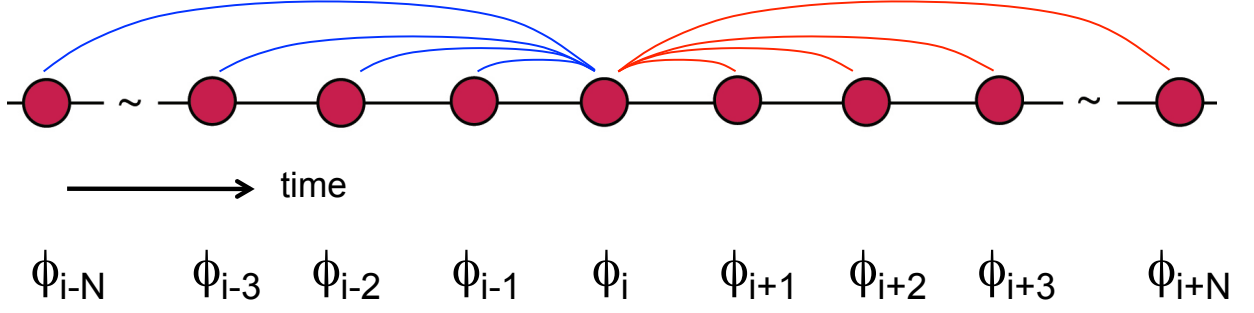
Figure 1: A diagram illustrating the common-point stacking algorithm to evaluate the propagation (atmospheric, ionospheric) and orbital contributions to the radar phase ϕ on an acquisition date i.

altitudes of about 50-1000km, while the tropospheric phase delays are dominated by variations in pressure and water content in the lowermost 10-20km of the atmosphere (*Bevis et al.* 1992). The methods proposed for the reduction of the propagation artifacts include averaging of multiple independent interferograms to suppress uncorrelated noise in the radar phase (*Fialko* 2006; *Peltzer et al.* 2001; *Wright et al.* 2004), spatio-temporal filtering (*Berardino et al.* 2002; *Ferretti et al.* 2001; *Schmidt and Bürgmann* 2003), wavelet decomposition (*Hetland et al.* 2012), as well as the use of auxiliary meteorologic and other data. Unfortunately, accurate estimates of water vapor in the atmosphere are not yet available at a sufficient spatiotemporal resolution worldwide. The same holds for estimates of the Total Electron Content (TEC) in th ionosphere that could be used to estimate ionospheric phase delays. We will use a new method for the calculation of noise due to atmospheric, ionospheric, and orbital artifacts directly from the SAR data (*Tymofyeyeva and Fialko* 2015). Our algorithm exploits the fact that interferograms that share a common scene necessarily contain the same contributions from delays in the radar phase due to propagation effects. The scheme entails the following steps:

1. Generate a set of interferograms for a given range of perpendicular baselines and time spans.
2. Select a subset of interferograms with sufficient correlation and coverage.
3. Evaluate Atmospheric Noise Coefficients (ANC) for each SAR acquisition. We do so by subdividing the interferometric "connectivity tree" into triplets, and computing the L_2 norm of range changes for every interferogram, as well as for sums of sequential interferograms sharing a common scene. The root mean square (RMS) of the de-trended range changes ($\Delta\rho$), defined as

$$RMS = \sqrt{\frac{1}{N}\sum_{i=0}^{N}(\Delta\rho_i - T_i)^2}, \tag{1}$$

where N is the number of valid pixels and T is some best-fitting trend (e.g., a quadratic surface, or some other predictor of zero mean), characterizes the power of the signal in each interferogram. Equation (2) illustrate how the Atmospheric Noise Coefficient (ANC) is defined for each acquisition:

$$ANC_i = (10.0)\ (R_{max})^{-1}\ \sqrt{\frac{1}{M}\sum_{m=1}^{M}(\alpha_i(x_m) - \overline{\alpha_i})^2} \tag{2}$$

where $\alpha_i(x_m)$ is the atmospheric phase delay at the pixel m on the date i, and $\overline{\alpha_i} = M^{-1}\sum_{m=1}^{M}\alpha_i(x_m)$ is the mean value of the atmospheric phase taken over all M pixels. R_{max} represents the RMS

3

(root mean square) value of the phase screen with the highest amount of noise, and is used to normalize the ANC values on a scale between 0 and 10. The ANC quantifies the relative amount of atmospheric noise at each SAR acquisition, and allows us to rank the acquisitions according to the magnitude of atmospheric contribution. In the next iteration, we recalculate α for each scene, starting with the noisiest date and using previously calculated atmospheric phase estimates to correct the interferograms used in the calculation of α for subsequent dates. The accuracy of the atmospheric phase estimates decreases toward the ends of the catalog, where shorter and/or one-sided averaging stencils need to be used. Such scenes are typically excluded from the subsequent time series analysis.

4. Compute atmospheric phase screens for all shared scenes by stacking interferograms that share the respective scene, making sure that the sign of interferograms that span later time periods is opposite to those of the earlier period, so that the atmospheric contribution is enhanced. Figure 1 illustrates the respective algorithm. We begin stacking for the atmospheric phase screens for the acquisitions with the largest ANCs. The computed phase screens are then subtracted from the interferograms used to estimate phase screens for the remaining acquisitions. The ANCs are then updated by computing RMS of the de-tended (zero-mean) atmospheric phase screens. The accuracy of the atmospheric phase estimates decreases toward the ends of the catalog, where shorter and/or one-sided averaging stencils need to be used. The procedure is repeated iteratively until the results converge with the prescribed tolerance.

Because ionospheric contributions and long-wavelength "ramps" due to incorrect orbital information have the same property of changing sign in the shared interferograms, they can be estimated using the same procedure. An essential point for the orbital error estimates is that the interferograms are not "flattened" during processing, and are generated using the original state vectors. This approach would be exact given a sufficiently large number of SAR acquisitions with regular intervals and good radar coherence between nearest data takes. Both conditions appear to be met in case of Sentinel-1 data.

We have validated our method by inverting synthetic data that contain realistic atmospheric noise and a known deformation signal, as well as by comparisons of InSAR and GPS time series (*Tymofyeyeva and Fialko* 2015). Among the limitations of the previous (ERS-1/2, ENVISAT, ALOS-1) data sets are uneven coverage from the ascending and descending orbits, and relatively narrow swathes (resulting in discontinuities in the LOS velocities across the swath boundaries). Sentinel-1 data are more optimal for generating a state-wide velocity field due to larger (by a factor of 3) swath width, and regular data takes.

We have processed all sequential Sentinel-1 interferograms that cover Southern California up to July 2018. Tightly controlled baselines of Sentinel-1 satellite(s) ensure that all acquisitions can be interfered with their immediate neighbors, thus providing sufficient information for continuous time series. Interferograms were processed using GMTSAR software (`topex.ucsd.edu/gmtsar`) with uniform parameters (e.g. adaptive filtering, SNAPHU unwrapping, 0.1 correlation threshold).

We have also produced secular rate estimates for several select tracks in the area of interest, and decomposed the LOS velocities into the vertical and horizontal components following the procedure described in *Lindsey et al.* (2014) and *Tymofyeyeva and Fialko* (2018). This procedure relies on an additional constraint on the azimuth of the horizontal displacement vector. This constraint is obtained from the interpolated horizontal (East and North) components of the velocity field provided by the continuous GPS data (*Tymofyeyeva and Fialko* 2018).

Figure 2 shows the resulting horizontal component of the secular velocity in the direction parallel to plate motion.

Figure 3 shows velocity profiles across the plate boundary spanning the Southern San Andreas Fault.
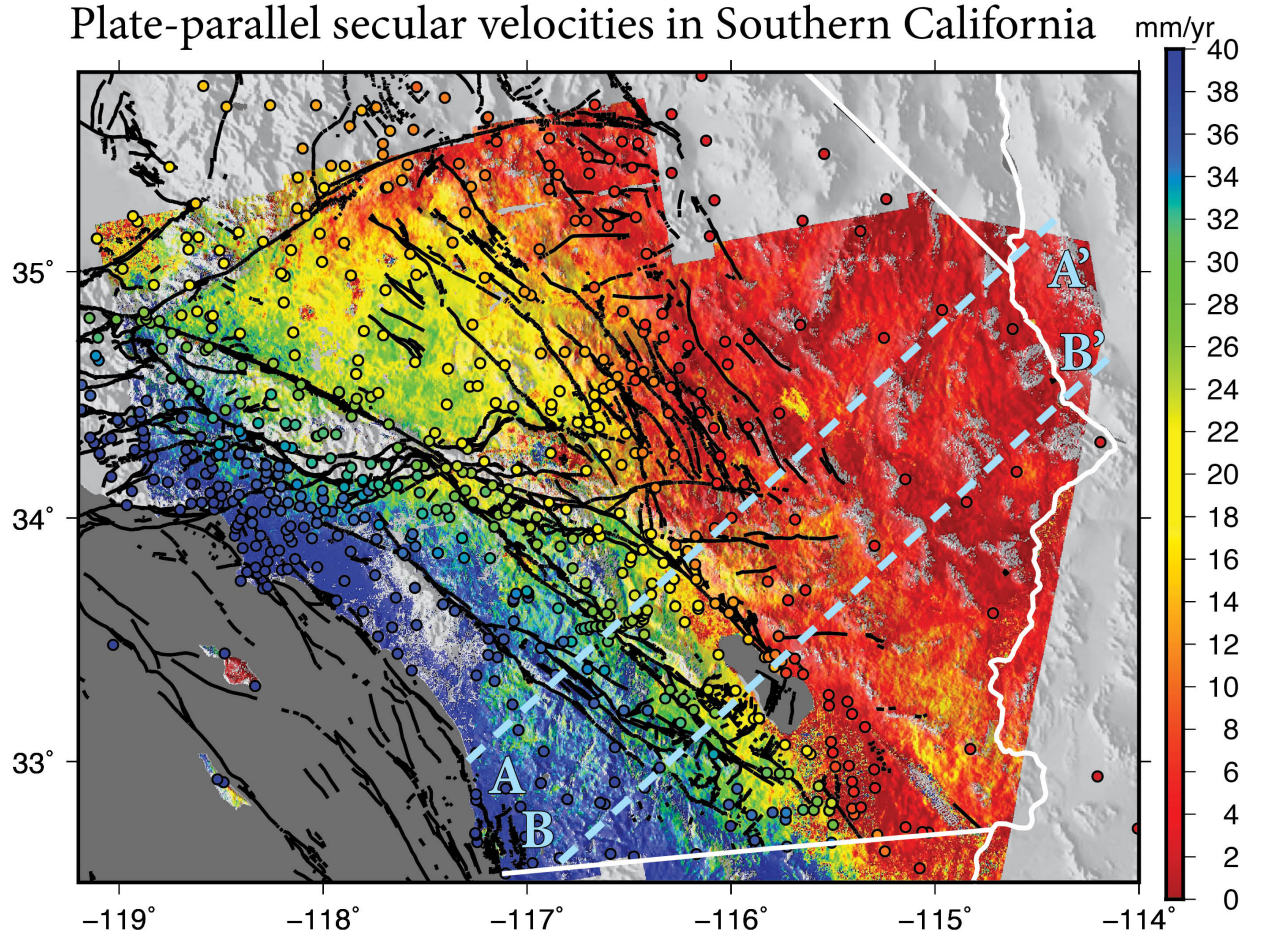
Figure 2: Secular velocity in the plate-parallel direction, calculated from the combination of ascending and descending Sentinel-1 acquisitions, and horizontal azimuths obtained from secular GPS velocities (CMM4). GPS velocities (colored circles) are plotted for comparison. Dashed blue lines indicate profiles across the plate boundary shown in Figure 3.
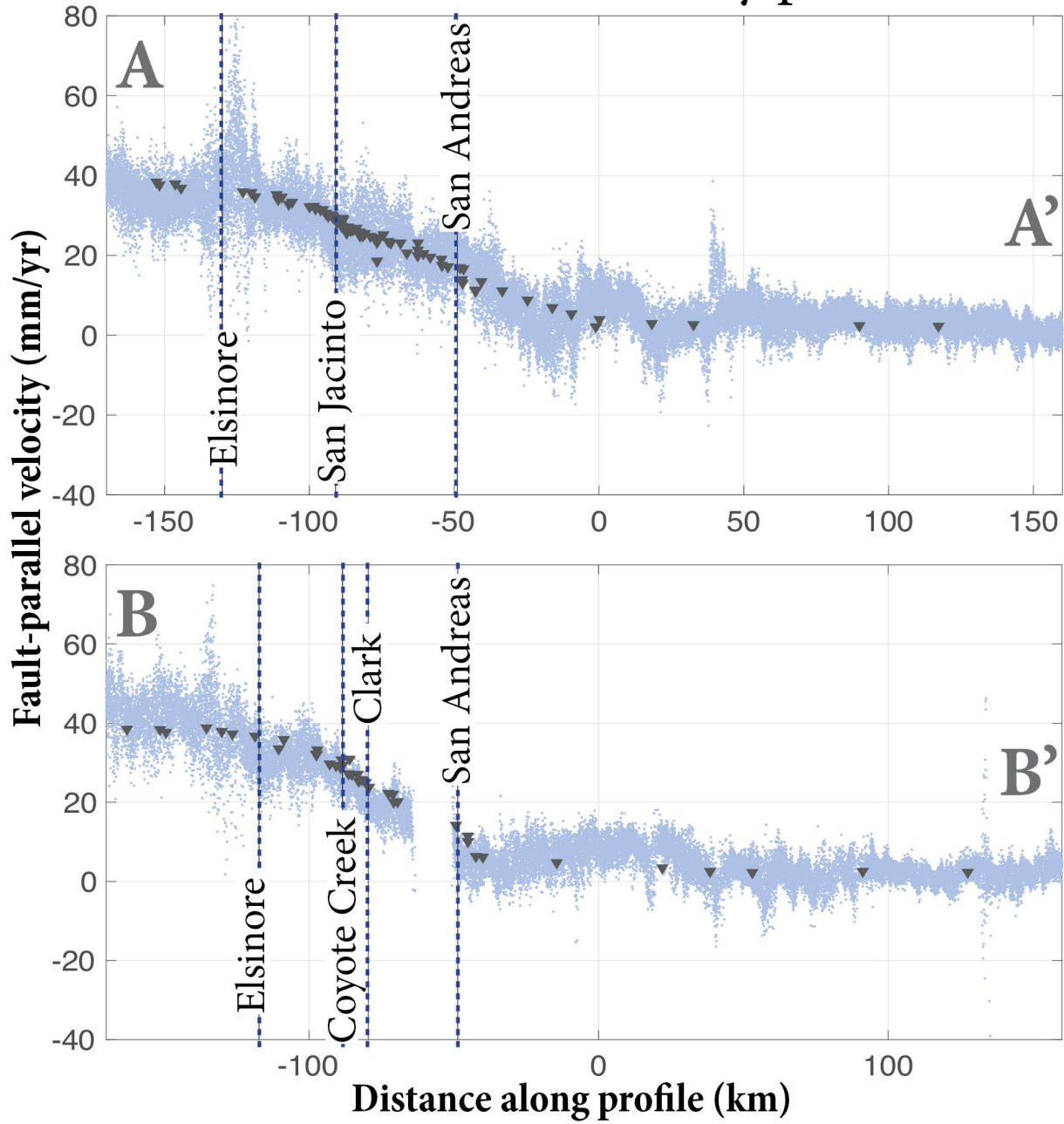
Figure 3: Horizontal velocities from profiles in Figure 2. Light blue dots: InSAR data, gray triangles: GPS data. Dashed vertical lines denote locations of major faults.

The resulting 3-component velocity maps provide a useful input into CGM. In particular, a robust and accurate characterization of vertical deformation of the Earth's surface is an important component of CGM, yet so far it has proven difficult as continuous GPS data are less sensitive to the vertical component of deformation compared to the horizontal component. The InSAR data are, on the other hand, highly sensitive to vertical motion. Thus an optimal combination of InSAR and GPS data is needed to produce a high-resolution map of vertical velocity over Southern California. The signal-to-noise ratio will further improve as more data are acquired in the next several years.

This project provided training and support for a female graduate student (Tymofyeyeva), who successfully defended her PhD at the end of Spring 2018 and moved on to a postdoc position at JPL/Caltech.

References

Berardino, P., G. Fornaro, R. Lanari, and E. Sansosti, A new algorithm for surface deformation monitoring based on small baseline differential SAR interferograms, *IEEE Transactions on Geoscience and Remote Sensing, 40*(11), 2375-2383, doi:10.1109/TGRS.2002.803792, 2002

Bevis, M., S. Businger, T. A. Herring, C. Rocken, R. A. Anthes, and R. H. Ware, GPS meteorology: Remote sensing of atmospheric water vapor using the global positioning system, *Journal of Geophysical Research, 97*(D14), 15,787, doi:10.1029/92JD01517, 1992

Burchfiel, B. C., K. V. Hodges, and L. H. Royden, Geology of Panamint Valley - Saline Valley Pull-Apart System, California: Palinspastic evidence for low-angle geometry of a Neogene Range-Bounding Fault, *Journal of Geophysical Research, 92*(B10), 10,422, doi:10.1029/JB092iB10p10422, 1987

Chen, Q., and J. Freymueller, Geodetic evidence for a near-fault compliant zone along the San Andreas Fault in the San Francisco Bay area, *Bulletin of the Seismological Society of America, 92*(2), 656-671, doi:10.1785/0120010110, 2002

Ding, X., Z. Li, J. Zhu, G. Feng, and J. Long, Atmospheric effects on InSAR measurements and their mitigation, *Sensors, 8*(9), 5426-5448, doi:10.3390/s8095426, 2008

Doin, M. P., C. Lasserre, G. Peltzer, O. Cavalié, and C. Doubre, Corrections of stratified tropospheric delays in SAR interferometry: Validation with global atmospheric models, *Journal of Applied Geophysics, 69*(1), 35-50, doi:10.1016/j.jappgeo.2009.03.010, 2009

Dokka, R., and C. Travis, Late Cenozoic strike-slip faulting in the Mojave Desert, California, *Tectonics, 9*(2), 311-340, doi:10.1029/TC009i002p00311, 1990

Ferretti, A., C. Prati, and F. Rocca, Permanent scatterers in SAR interferometry, *IEEE Transactions on Geoscience and Remote Sensing, 39*(1), 8-20, doi:10.1109/36.898661, 2001

Fialko, Y., Probing the mechanical properties of seismically active crust with space geodesy: Study of the coseismic deformation due to the 1992 Mw7.3 Landers (southern California) earthquake, *Journal of Geophysical Research, 109*(B3), B03307, doi:10.1029/2003JB002756, 2004a

Fialko, Y., Evidence of fluid-filled upper crust from observations of postseismic deformation due to the 1992 Mw7.3 Landers earthquake, *Journal of Geophysical Research, 109*(B8), B08,401, doi:10.1029/2004JB002985, 2004b

Fialko, Y., Interseismic strain accumulation and the earthquake potential on the southern San Andreas fault system, *Nature, 441*(7096), 968-71, doi:10.1038/nature04797, 2006

Fialko Y., D. Sandwell, D. Agnew, M. Simons, and B. Minster, Deformation on nearby faults induced by the 1999 Hector Mine earthquake, *Science (New York, N.Y.), 297*(5588), 1858-62, doi:10.1126/science.1074671, 2002

Fialko, Y., D. Sandwell, M. Simons, and P. Rosen, Three-dimensional deformation caused by the Bam, Iran, earthquake and the origin of shallow slip deficit, *Nature, 435*(7040), 295-9, doi:10.1038/nature03425, 2005

Foster, J., B. Brooks, T. Cherubini, C. Shacat, S. Businger, and C. L. Werner, Mitigating atmospheric noise for InSAR using a high resolution weather model, *Geophysical Research Letters, 33*(16), L16,304, doi:10.1029/2006GL026781, 2006

Fournier, T., M. E. Pritchard, and N. Finnegan, Accounting for atmospheric delays in InSAR data in a search for long-wavelength deformation in South America, *IEEE Transactions on Geoscience and Remote Sensing, 49*(10), 3856-3867, doi:10.1109/TGRS.2011.2139217, 2011

Goldstein, R., Atmospheric limitations to repeat-track radar interferometry, *Geophysical Research Letters, 22*(18), 2517-2520, doi:10.1029/95GL02475, 1995

Gong, W., F. J. Meyer, S. Liu, and R. F. Hanssen, Temporal Filtering of InSAR Data Using Statistical Parameters From NWP Models, *IEEE Transactions on Geoscience and Remote Sensing, 53*(7), 4033,4044, doi:10.1109/TGRS.2015.2389143, 2015

Hetland, E. A., P. Musé, M. Simons, Y. N. Lin, P. S. Agram, and C. J. DiCaprio, Multi-scale InSAR Time Series (MInTS) analysis of surface deformation, *Journal of Geophysical Research, 117*(B2), B02,404, doi:10.1029/2011JB008731, 2012

Jehle, M., O. Frey, D. Small, and E. Meier, Measurement of ionospheric TEC in spaceborne SAR data, *IEEE Transactions on Geoscience and Remote Sensing, 48*(6), 2460-2468, doi:10.1109/TGRS.2010.2040621, 2010

Jolivet, R., P. S. Agram, N. Y. Lin, M. Simons, M. P. Doin, G. Peltzer, and Z. Li, Improving InSAR geodesy using global atmospheric models, *Journal of Geophysical Research: Solid Earth, 119*(3), 2324-2341, doi:10.1002/2013JB010588, 2014

Jónsson, S., P. Segall, R. Pedersen, and G. Björnsson, Post-earthquake ground movements correlated to pore-pressure transients, *Nature, 424*(6945), 179-83, doi:10.1038/nature01776, 2003

Kaneko, Y., Y. Fialko, D. T. Sandwell, X. Tong, and M. Furuya, Interseismic deformation and creep along the central section of the North Anatolian Fault (Turkey): InSAR observations and implications for rate-and-state friction properties, *Journal of Geophysical Research: Solid Earth, 118*(1), 316-331, doi:10.1029/2012JB009661, 2013

Li, Z., X. Ding, C. Huang, G. Wadge, and D. Zheng, Modeling of atmospheric effects on InSAR measurements by incorporating terrain elevation information, *Journal of Atmospheric and Solar-Terrestrial Physics, 68*(11), 1189-1194, doi:10.1016/j.jastp.2006.03.002, 2006

Lindsey, E., Y. Fialko, Y. Bock, D. Sandwell, R. Bilham, Localized and distributed creep along the southern San Andreas Fault, *J. Geophys. Res., 119*, 7909-7922, 2014

Lindsey, E. O., V. J. Sahakian, Y. Fialko, Y. Bock, S. Barbot, and T. K. Rockwell, Interseismic Strain Localization in the San Jacinto Fault Zone, *Pure and Applied Geophysics, 171*(11), 2937-2954, doi:10.1007/s00024-013-0753-z, 2013

Meyer, F. J., Performance requirements for ionospheric correction of low-frequency SAR data, *IEEE Transactions on Geoscience and Remote Sensing, 49*(10), 3694-3702, doi:10.1109/TGRS.2011.2146786, 2011

Peltzer, G., P. Rosen, F. Rogez, and K. Hudnut, Poroelastic rebound along the Landers 1992 earthquake surface rupture, *Journal of Geophysical Research, 103*(B12), 30131 doi: 10.1029/98JB02302, 1998

Peltzer, G., F. Crampé, S. Hensley, and P. Rosen, Transient strain accumulation and fault interaction in the Eastern California Shear Zone, *Geology, 29*(11),975, 2001

Sauber, J., W. Thatcher, and S. C. Solomon, Geodetic measurement of deformation in the central Mojave Desert, California, *Journal of Geophysical Research, 91*(B12), 12683, doi:10.1029/JB091iB12p12683, 1986

Savage, J.C., and R. O. Burford, Geodetic determination of relative plate motion in central California, *Journal of Geophysical Research, 78*(5), 832-845, doi:10.1029/JB078i005p00832, 1973

Schmidt, D. A., and R. Bürgmann, Time-dependent land uplift and subsidence in the Santa Clara valley, California, from a large interferometric synthetic aperture radar data set, *Journal of Geophysical Research, 108*(B9), 2416, doi:10.1029/2002JB002267, 2003

Tarayre, H., and D. Massonnet, Atmospheric propagation heterogeneities revealed by ERS-1 interferometry, *Geophysical Research Letters, 23*(9), 989-992, doi:10.1029/96GL00622, 1996

Tymofyeyeva, E. and Y. Fialko, Mitigation of atmospheric phase delays in InSAR data, with application to the Eastern California Shear Zone, *J. Geophys. Res., 120*, 5952-5963, 2015

Tymofyeyeva, E. and Y. Fialko, Geodetic evidence for a blind fault segment at the Southern end of the San Jacinto Fault Zone, *J. Geophys. Res., 123*, 878-891, 2018

Wadge, G., M. Zhu, R. Holley, I. James, P. Clark, C. Wang, and M. Woodage, Corrections of atmospheric delay effects in radar interferometry using a nested mesoscale atmospheric model, *Journal of Applied Geophysics, 72*(2), 141-149, doi:10.1016/j.jappgeo.2010.08.005, 2010

Wright, T. J., B. Parsons, P. C. England, and E. J. Fielding, InSAR observations of low slip rates on the major faults of western Tibet, *Science (New York, N.Y.), 305*(5681), 236-9, doi:10.1126/science.1096388, 2004

Zebker, H. A., P. A. Rosen, and S. Hensley, Atmospheric effects in interferometric synthetic aperture radar surface deformation and topographic maps, *Journal of Geophysical Research, 102*(B4), 7547, doi:10.1029/96JB03804, 1997